Observation of the Effects of Radially Sheared Electric Fields on the Suppression of Turbulent Vortex Structures and the Associated Transverse Loss in GAMMA 10

doi: 10.1103/PhysRevLett.94.085002

Observation of the Effects of Radially Sheared Electric Fields on the Suppression of Turbulent Vortex Structures and the Associated Transverse Loss in GAMMA 10

T. Cho,[1] M. Yoshida,[1] J. Kohagura,[1] M. Hirata,[1] T. Numakura,[1] H. Higaki,[1] H. Hojo,[1] M. Ichimura,[1] K. Ishii,[1] K. Md. Islam,[1] A. Itakura,[1] I. Katanuma,[1] Y. Nakashima,[1] T. Saito,[1] Y. Tatematsu,[1] M. Yoshikawa,[1] Y. Kojima,[1] S. Tokioka,[1] N. Yokoyama,[1] Y. Tomii,[1] T. Imai,[1] V. P. Pastukhov,[2] S. Miyoshi,[1] and GAMMA 10 Group[1]

[1]*Plasma Research Center, University of Tsukuba, Tsukuba, Ibaraki 305-8577, Japan*

[2]*Russian Research Center "Kurchatov Institute," Moscow, Russia*

(Received 25 July 2004; published 3 March 2005)

Vortexlike turbulent structures in hot-ion mode plasmas with several keV are observed in the case with a radially produced weak shear of electric fields E_r. However, a strong E_r shear formation due to a high ion-confining potential ϕ_c production clears up these vortices together with plasma-confinement improvement and disappearance of both drift-wave and turbulencelike Fourier spectral signals. These findings are based on three-time progress in ϕ_c in comparison to ϕ_c attained 1992–2002. The significant advance of ϕ_c is well extended in line with proposed potential-formation physics scalings.

DOI: 10.1103/PhysRevLett.94.085002 PACS numbers: 52.55.Jd, 52.25.Fi, 52.35.Ra, 52.70.La

Experimental verification of the effects of the formation of radially sheared electric fields E_r (or potentials) in plasmas is one of the most critical issues to understand physics bases for plasma-confinement improvements found in various types of devices. One of the most essential and inherent characteristic advantages of open-ended mirror devices [1–9] is the ease of control of a radial potential distribution and the associated E_r shear profile or the frequency of a nonuniform sheared plasma rotation [$\Omega_r = E_r/(r_c B)$] profile. Such a control of Ω_r or E_r in mirror devices is easily carried out on the basis of driving axial fast electron flows from plug electron-cyclotron heating (ECH) regions [8,9] into open-ended mirror regions along the lines of magnetic force [8–13]. (Here, r_c denotes a radius mapped to the central cell.) Thus, the profile control of the axial electron flows due to ECH power control of the radial distribution and intensity (see below) provides a convenient "active control" method of the shear profile. This allows for flexible and advantageous mirror experiments for constructing common relations between the shear profiles and reductions in fluctuation-driven radial plasma losses (or transverse confinement) along with physics details of interior hot-plasma behavior.

Recently, three-time progress in the formation of ion-confining potentials ϕ_c including a record of 2.1 kV in the plug region (filled circles in Fig. 1), in comparison to ϕ_c attained 1992–2002 [14,15] (open circles in Fig. 1), is achieved in a hot-ion mode [14–17] having bulk-ion temperatures $T_i =$ several keV. The advance in the potential formation leads to a finding of remarkable effects of sheared E_r (i.e., $E_r' = dE_r/dr \approx$ several 10 kV/m^2) or sheared Ω_r on the suppression of not only a coherent drift-wave-relevant Fourier component but also broadband turbulencelike fluctuations (or vortexlike structures; see below) in GAMMA 10. Here, the progress in the potential formation is made in line with the extension of our proposed scaling of ϕ_c with powers of plug (P_{PECH}) and barrier (P_{BECH}) ECH [14,15] (see the data fit to the scaling surface in Fig. 1) covering representative tandem-mirror operational modes, characterized in terms of a high-potential mode having kV-order plasma-confining potentials [5,8,9] and a hot-ion mode yielding fusion neutrons with $T_i = 10$–20 keV [17].

The progress of higher ϕ_c formation in turn gives bases for the following remarkable effects of the formation of a strong central cell E_r or Ω_r *shear,* since the shear is proportional to the central cell (Φ_C) and plug (Φ_P) potentials. Along the lines of magnetic force, Φ_C is closely connected with and raised by a Φ_P rise due to plug ECH having the Gaussian power-lobe profile of $P_{\mathrm{ECH}}(0) \times \{\exp[-(r_c/a)^2]\}$. In fact, such a proportionality of Φ_C to

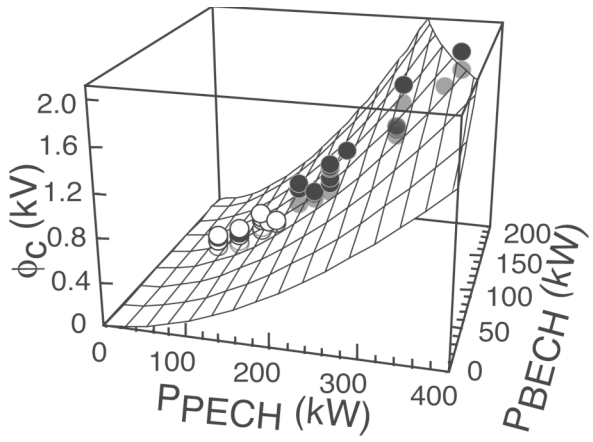

FIG. 1. Three-time advance in ϕ_c including a record of 2.1 kV (filled circles), in comparison to ϕ_c attained 1992–2002 (open circles), extensionally fits well to the scaling surface of ϕ_c with plug (P_{PECH}) and barrier (P_{BECH}) ECH powers (see Refs. [14,15]). Here, $n_c = 2 \times 10^{18}$ m^{-3} is exemplified for a tandem-mirror configuration with $n_p/n_c = 0.1$ and $T_i =$ several keV.

Φ_P is experimentally observed [11,12]. Here, (0) indicates values at $r_c = 0$, and Φ and ϕ denote the absolute value and difference of potentials, respectively.

Nonuniform plasma rotation can suppress existing plasma instabilities and fluctuations. As a result, the considerable reduction of cross-field plasma transport is expected. Analyzing results of Ref. [18] and other aspects of the problem (in particular, see subsections 1.6.2 and 2.1.1 in Ref. [18]) provide the value $W_r = [\nabla \times (nV_E)]_z/n(0) = (nr_c^2\Omega_r)'/[n(0)r_c]$ (i.e., the z component of the normalized vorticity of plasma momentum density) as an appropriate measure of the $E \times B$ velocity (V_E) shear in the case of rotating plasmas with nonuniform density profiles. [For slab flows with a uniform density, $W_{\mathrm{slab}-x} = dV_E/dx$, and $W_r = (2/B)[n/n(0)](dE_r/dr)$ for the cylindrical geometry having the same e-folding lengths of the Gaussian profiles for n and Φ_c.]

Here, we outline the GAMMA 10 device. It is a minimum-B anchored tandem mirror with outboard axisymmetric plug and barrier cells [5,8,9], having an axial length of $z = 27$ m, and the total volume of the vacuum vessel of 150 m^3. The central cell has a length of 6 m and a limiter with a diameter of 36 cm, and the magnetic-field intensity at the midplane $B_z = B_m$ is 0.405 T with a mirror ratio R_m of 5.2. Ion-cyclotron heatings (ICH) (200 kW at 4.47 or 6.36 MHz, as well as 100 kW at 9.9 or 10.3 MHz) are employed for the central-cell hot-ion production and the anchor stabilization, respectively [19,20]. The plug and barrier cells are axisymmetric mirrors; they have an axial length of 2.5 m ($B_m = 0.497$ T, and $R_m = 6.2$). Microwaves at 28 GHz are injected in the extraordinary mode into the plug and the barrier regions to produce ϕ_c and a thermal-barrier potential ϕ_b, respectively. Absolute values of Φ_P are measured with our originally developed electrostatic end-loss ion-energy spectrometer (IES) arrays [21]. Barrier potentials Φ_B and Φ_C are directly measured with heavy-ion (Au^0) beam probes (HIBP) [22]. Therefore, one can obtain ϕ_c and ϕ_b as $\Phi_P - \Phi_C$ and $\Phi_C - \Phi_B$, respectively.

In Fig. 2(a), the central-cell line density nl_c of a hot-ion mode plasma with $T_i = 4$ keV increases during plug ECH in association with reducing fluctuations. Various fluctuation diagnostics, including a movable microwave interferometer, the Fraunhofer-diffraction method [23], two sets of developed 50-channel soft x-ray detectors using microchannel plates [9,10,24] in the central-cell midplane, eight Langmuir probes (i.e., every 45° at $r_c = 18$ cm in the central cell) for wave phasing and coherence diagnostics [20], the above-described HIBP [22], and eight sets of IES (for more detail, see Ref. [21]), as well as simultaneous potential diagnostics with HIBP and IES, show consistently the same characteristic features as described below.

At first, two data sets, one before [Figs. 2(b)–2(f)] and one during [Figs. 2(g)–2(k)] ECH ($P_{\mathrm{ECH}} = 180$ kW), are compared. Frequency analyses of IES signals, for instance, are shown in Fig. 2(b). The existence of electron drift waves with the *coherent* mode numbers $m = 1, 2, \ldots$ [20,23], giving a peaked structure (see arrows) over a few kHz [23], and broadband *turbulent fluctuations* having *incoherent* azimuthal phase relations are found. In Figs. 2(e) and 2(j), W_r deduced from measurements of the density profile and Φ_C with IES and HIBP is plotted. It is found that a weak shear is formed in the case without ECH [Fig. 2(e)]. On the other hand, a data set during ECH [Figs. 2(g)–2(k)] having a stronger shear [Fig. 2(j)] shows a significant difference. Figures 2(h) and 2(i) show a considerable reduction of fluctuations over all radii, and particularly near the plasma axis and $r_c \approx 10$ cm, where the shear has the maximal values. Nevertheless, an appreciable level of fluctuations still exists at about $r_c = 6$–7 cm, where no shear is formed. [Here, for reference, both E_r shear and W_r values are plotted (see above).]

In Figs. 2(m)–2(q), a similar data set to that in Figs. 2(b)–2(f) having turbulence is obtained, although ECH ($P_{\mathrm{ECH}} = 120$ kW) is applied in Figs. 2(m)–2(q) as in Figs. 2(g)–2(k). However, remarkably different behavior is found in these two data sets. As one can see in Fig. 2(p), a weaker shear than that in Fig. 2(j) is formed.

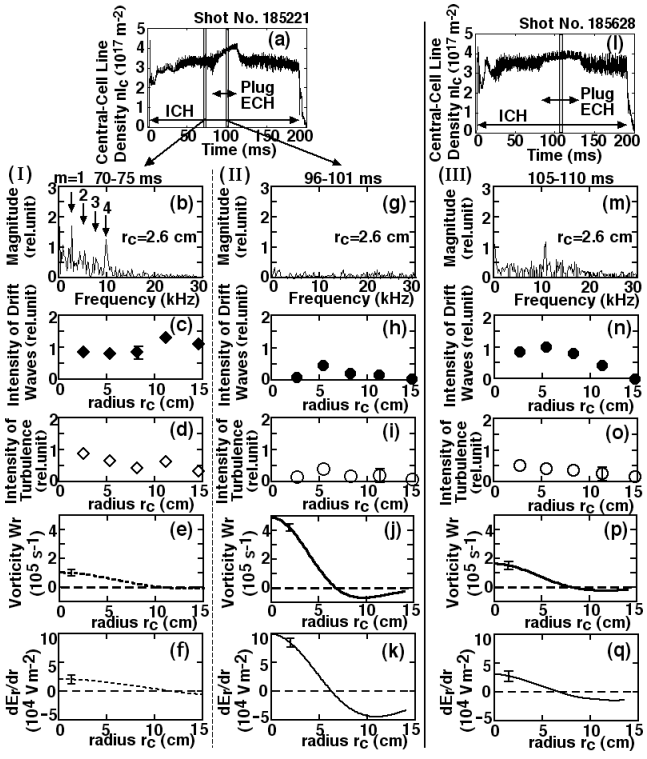

FIG. 2. Data sets of (I) ICH plasmas having a weak shear (a small W_r) (b)–(f), and (II) with plug ECH (180 kW) producing a strong shear (a large W_r) (g)–(k). In (b), Fourier components of coherent drift waves with mode numbers m (see Ref. [23]) and broadband incoherent turbulent signals for IES, for instance, are suppressed in (g)–(k) except at $r_c \approx 6$–7 cm having approximately zero shear. (III) Another data set during weaker plug ECH (120 kW) in (l)–(q) having a weaker shear as compared to that in (g)–(k). Noisier and earlier saturated density rise in (l) during ECH is found in comparison to that in (a).

For this weak shear, a lower-level saturation of density rise is found during ECH [Fig. 2(l)] with stronger density fluctuations [compare nl_c in Fig. 2(a) during ECH].

The difference in the density rise in Figs. 2(a) and 2(l) is carefully investigated by the use of a widely employed particle-balance equation, $edN/dt = I_s - I_{\parallel} - I_{\perp}$ [1,4,5,9,12,23]. Here, the contribution of nonambipolar $I_{\perp}$ to total $I_{\perp}$ is observed to be ignorable as compared to ambipolar $I_{\perp}$ by using floated end plates having $\approx M\Omega$ resistance (for more details, see Ref. [25]). In Fig. 3(a), a rising rate edN/dt of the total particle number N during ECH [see Fig. 2(a)] integrated along a specific axial flux tube well balances the difference between particle source currents I_s deduced from H_{α} detector-array data and an axial-loss current $I_{\parallel}$ from IES placed along the corresponding flux tube (for more details, see Refs. [1,5,12,23]). It is noted that $I_{\parallel}$ is obtained from the envelope of "saw-toothed" end-loss signals in Fig. 3(b) because of a sinusoidal ion-repeller biasing for IES [21]. This shows negligible $I_{\perp}$. The property of $I_{\parallel} \gg I_{\perp}$ is consistently confirmed by good agreement between the data on $I_{\parallel}$ in Fig. 3(b) and Pastukhov's theoretically evaluated $I_{\parallel}$ [filled circles in Fig. 3(b)], since the Pastukhov theory [7] predicts $I_{\parallel}$ under the assumption of negligible $I_{\perp}$.

On the other hand, the data in Figs. 3(c) and 3(d) correspond to the data set in Figs. 2(l)–2(q). By the use of the same methods, an appreciable amount of $I_{\perp}$ [see diamonds in Fig. 3(c) during ECH, as compared with those in Fig. 3(a) during ECH] is found; for instance, $I_{\perp} \approx (1/2)I_{\parallel}$ at $t = 100$ ms in Fig. 3(c). It is also noted that $I_{\parallel}$ observed at $t = 100$ ms in Fig. 3(d) ranges consistently about 2/3 of Pastukhov's predicted $I_{\parallel}$. The remainder of 1/3 of the predicted $I_{\parallel}$ is interpreted by the radial losses $I_{\perp}$ before the axial-loss currents reach mirror-end regions. This is consistent with the fact of an earlier saturation of nl_c in Fig. 2(l) in comparison to its continuous rise in Fig. 2(a) during ECH having a strong shear. Similar behavior is also found before ECH [at $t = 75$ ms in Fig. 2(a)] associated with drift waves and turbulent signals [Figs. 2(b)–2(f)] having a weak shear. Again, the particle balance requires an appreciable $I_{\perp}$ [Fig. 3(a)] along with disagreement between the predicted $I_{\parallel}$ and the data on $I_{\parallel}$ in Fig. 3(b).

For identifying the spatial behavior and structure of turbulence signals [Fig. 2(b)] with a weak shear [Figs. 2(e) or 2(p)], in comparison to those with a strong shear [Fig. 2(j)], contours of the central-cell soft x-ray brightness I_{sx} are shown in Figs. 4(a) and 4(b). "Hot-colored" regions indicate higher plasma-pressure locations. One can find spatially and temporally varied turbulent vortexlike structures during a weaker shear period [Fig. 4(b)] in the absence of ECH [Figs. 2(b)–2(f)]. These turbulent structures are, however, going to clear up

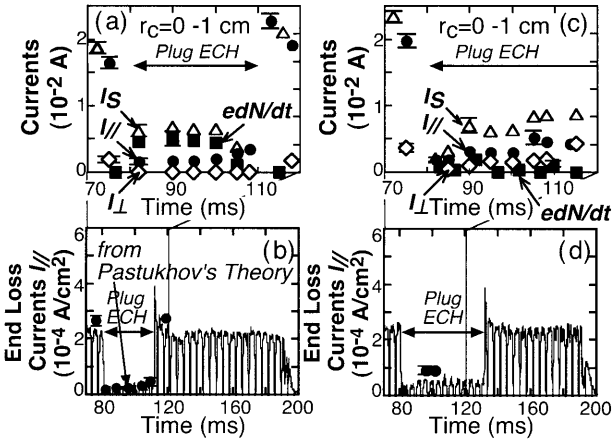

FIG. 3. Improved confinement having a strong shear during ECH in Figs. 2(g)–2(k) is analyzed from (a) a particle-balance equation; no appreciable transverse loss $I_{\perp}$ and consistently good agreement with (b) Pastukhov's predicted $I_{\parallel}$ (filled circles) are found. On the other hand, poor confinement with a weak shear [Figs. 2(l)–2(q)] is accompanied by an appreciable $I_{\perp}$ in (c). [Here, $I_{\perp} = (1/2)I_{\parallel}$ at $t = 100$ ms in (c), for instance.] Also, $I_{\parallel}$ at $t = 100$ ms in (d) is consistently about 2/3 of Pastukhov's predicted $I_{\parallel}$. The remainder of $I_{\parallel}$ is interpreted by $I_{\perp}$ before reaching mirror ends. This is consistent with an earlier saturation of nl_c in Fig. 2(l) as compared to its continuous rise in Fig. 2(a) during ECH with a strong shear.

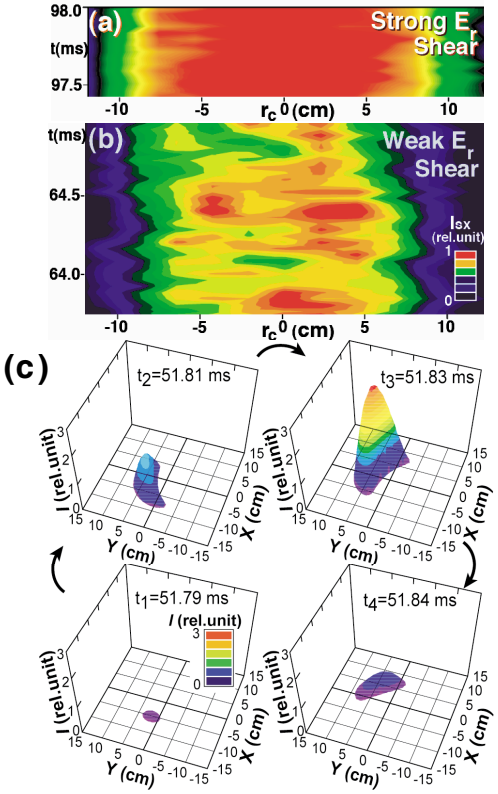

FIG. 4 (color). Contours of central-cell x-ray brightness in the cases with (a) strong and (b) weak E_r shear formation. "Hot-colored areas" show higher plasma-pressure locations. Vortexlike structures are found in (b). The temporal evolution of a vortex is exemplified in (c) by the use of our developed x-ray tomography systems. ($I \propto n_e n_i T_e^{2.3}$.)

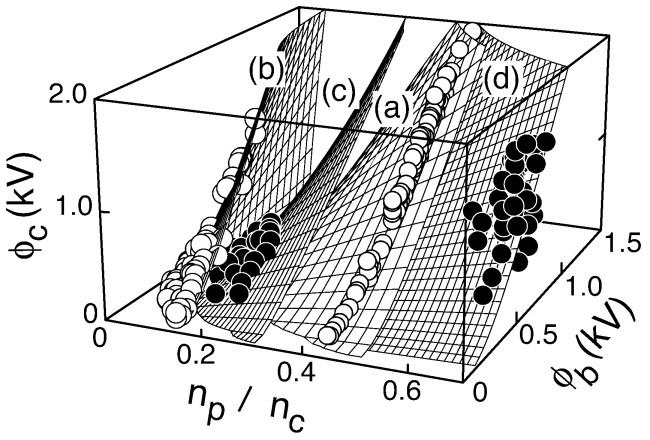

FIG. 5. The validity of theoretical surfaces for potential formation [16] covering (a) the high-potential and (b) hot-ion modes is extensionally investigated by using the advanced data for constructing potential physics interpretations and controlling potential enhanced E_r shear. Data well fit to surfaces (c) and (d) for the modes of (b) and (a) with central ECH, respectively, along with (d) plug NBI.

with ECH [Fig. 4(a)] together with the simultaneous disappearance of the broadband Fourier component [compare Fig. 2(b) with Fig. 2(g)] as well as a temperature rise [Fig. 4(a)]. A combination of x-ray data from the above-described detector array and another one having a 135° separation in the central midplane allows us to reconstruct a detailed vortex structure [Fig. 4(c)]. Its typical lifetime from formation to disappearance ranges 100 μs with a rotational motion of an $E_r \times B_z$ drift approximately. In Fig. 4(c), the center of the vortexlike structure appears at $r_c \approx 5$ cm and is faded at $r_c \approx 7$ cm into a detector noise level. Consequently, the existence of such vortexlike turbulent phenomena may provide a correlation with the appearance of the above-described additional transport $I_\perp$ with confinement degradation [Figs. 3(c), 3(d), and 4(b)] in the case with a weak shear formation, while these turbulence phenomena disappear and confinement is improved with a strong shear formation [Figs. 3(a), 3(b), and 4(a)]. From a common physics viewpoint, such investigations by using easy controllability of E_r shear in mirror devices may provide an opportunity for exploring extended and generalized cooperation researches related to the mechanism identification of the H-mode pedestal, the blob, and the internal transport-barrier formation [26].

Finally, for constructing physics interpretations and control methods of such potential and the associated E_r shear formation, the validity of our proposed potential mechanism [16] for (a) the high-potential and (b) hot-ion modes is extensionally tested in Fig. 5. The surfaces in Fig. 5 are calculated from the strong ECH theory (plateau formation) [6] in combination with the generalized Pastukhov's theory on energy confinement [7] (for more detail, see Ref. [16]). Central ECH, increasing electron axial flows from the central cell into the plug regions over ϕ_b, provides an increase in the density ratio of the plug to central regions, n_p/n_c. In Fig. 5, as found on the surfaces (c) and (d) with central ECH along with (d) additional plug neutral beam injections (NBI), the validity is still confirmed under these auxiliary-heating conditions.

In summary, three-time progress in the formation of ϕ_c including a record of 2.1 kV is achieved in the hot-ion mode in comparison to ϕ_c attained 1992–2002 [14,15] (Fig. 1). The advance in the potential formation leads to a finding of remarkable effects of a strong E_r shear or W_r on the suppression of not only coherent drift waves but also vortexlike turbulent fluctuations (Figs. 2 and 4) in association with confinement improvement (Fig. 3). The progress in the potential formation is made in line with the extension of proposed physics scalings [16] (Fig. 5).

[1] R. F. Post, Nucl. Fusion **27**, 1579 (1987), a review paper of mirrors; Trans. Fusion Sci. Technol. **43**, 195 (2003).
[2] D. D. Ryutov, in *Proceedings of the International Conference on Plasma Physics, New Delhi, 1989* (IAS, Bangalore, 1989).
[3] A. C. England *et al.*, Trans. Fusion Sci. Technol. **43**, 73 (2003); M. Kwon *et al.*, *ibid.* **43**, 23 (2003).
[4] N. Hershkowitz, S. Miyoshi, and D. D. Ryutov, Nucl. Fusion **30**, 1761 (1990).
[5] S. Miyoshi *et al.*, Fiz. Plazmy **23**, 781 (1997) [Plasma Phys. Rep. **23**, 723 (1997)].
[6] R. H. Cohen, Phys. Fluids **26**, 2774 (1983).
[7] V. P. Pastukhov, Nucl. Fusion **14**, 3 (1974); R. H. Cohen *et al.*, Nucl. Fusion **18**, 1229 (1978); **19**, 1295 (1979); **19**, 1693 (1979).
[8] T. Cho *et al.*, Phys. Rev. Lett. **64**, 1373 (1990).
[9] T. Cho *et al.*, Phys. Rev. A **45**, 2532 (1992).
[10] T. Cho *et al.*, Nucl. Fusion **27**, 1421 (1987).
[11] T. Kariya *et al.*, Phys. Fluids **31**, 1815 (1988).
[12] T. Cho *et al.*, Nucl. Fusion **28**, 2187 (1988).
[13] T. Cho *et al.*, Nucl. Fusion **41**, 1161 (2001).
[14] T. Cho *et al.*, in *Proceedings of the 19th IAEA Fusion Energy Conference, Lyon, 2002* (IAEA, Vienna, 2003).
[15] T. Cho *et al.*, Nucl. Fusion **43**, 293 (2003).
[16] T. Cho *et al.*, Phys. Rev. Lett. **86**, 4310 (2001).
[17] Y. Kiwamoto *et al.*, Phys. Plasmas **3**, 578 (1996).
[18] A. V. Timofeev, *Review of Plasma Physics* (Consultants Bureau, New York, 1992), Vol. 17, pp. 193–301.
[19] M. Ichimura *et al.*, Nucl. Fusion **39**, 1995 (1999).
[20] S. Tanaka *et al.*, Rev. Sci. Instrum. **70**, 979 (1999).
[21] M. Yoshida *et al.*, Rev. Sci. Instrum. **74**, 1909 (2003).
[22] K. Ishii *et al.*, Rev. Sci. Instrum. **60**, 3270 (1989).
[23] A. Mase *et al.*, Phys. Rev. Lett. **64**, 2281 (1990); Nucl. Fusion **31**, 1725 (1991).
[24] M. Hirata *et al.*, Nucl. Instrum. Methods Phys. Res., Sect. B **66**, 479 (1992).
[25] I. Katanuma *et al.*, Nucl. Fusion **27**, 2041 (1987).
[26] Y. Kishimoto *et al.*, Nucl. Fusion **40**, 667 (2000), and references therein.